Numerical Calculation of the Three Dimensional Inter-Bar Current Distribution in Induction Machines

J. Güdelhöfer, R. Gottkehaskamp and A. Möckel

***Abstract*—The proposed numerical model is used to study the influence of inter-bar currents by investigating the three dimensional field solution in COMSOL Multiphysics. Since the focus is on the rotor, the whole stator geometry is replaced by surface current densities in terms of Neumann boundary conditions. This includes the winding heads. An alternative way of modelling the rotor lamination is presented. All iron sheets are replaced by one domain. The simplifications help to reduce the size and by this also the effort to solve the model.**

The results show that the motors operating behaviour changes dramatically over the range of the inter-bar resistance. With the chosen approach to respect the rotor stacking, it is possible to investigate the behaviour of inter-bar currents for different rotor laminations. According to the results, the stacking only has a small influence on the inter-bar currents.

I. Nomenclature

μ	magnetic permeability
∇	nabla operator
$\vec{A}$	magnetic vector potential
φ	electric scalar potential
κ	electric conductivity
$\vec{D}$	electric displacement field
$\vec{E}$	electric field
$\vec{J}$	current density
$\vec{J}_\mathrm{e}$	external current density
$\vec{j}$	surface current density
r_q	inter-bar resistivity
U	RMS value of the voltage over one phase
R_1	Resistance of one phase
$L_{1,1}$	Self inductance of one phase
I	RMS value of the current in one phase
$M_{2,1}$	Mutual inductance between stator and rotor
I_R	RMS value of the ring current
R_2	Resistance of one rotor loop
$L_{2,2}$	Self inductance of one rotor loop
f	frequency
ν_max	maxmimum harmonic number
Φ	Flux through one phase
Ψ	Flux linkage of one phase
k_w	winding factor
w	number of turns of one phase
$L_{\sigma,\mathrm{dl}}$	leakage inductance of the airgap field
L_N1	leakage inductance of the stator slot
L_S1	leakage inductance of the winding heads in the stator

J. Güdelhöfer is with the Faculty of Electrical & Information Technology, University of Applied Sciences Düsseldorf, Düsseldorf, Germany (e-mail: jan.guedelhoefer@hs-duesseldorf.de).

R. Gottkehaskamp is with the Faculty of Electrical & Information Technology, University of Applied Sciences Düsseldorf, Düsseldorf, Germany (e-mail: raimund.gottkehaskamp@hs-duesseldorf.de).

A. Möckel is with the Small Electrical Drives Group, Technical University of Ilmenau, Ilmenau, Germany (email: andreas.moeckel@tu-ilmenau.de).

II. Introduction

Induction motors combine robustness and simple rotor structures. As a result, they are the most spread motor topology world wide. Raising energy costs and environmental awareness might lead to a loss of this top position in the future. The reason for this is that induction motors lack efficiency, compared to other topologies, like permanent magnet synchronous motors or synchronous reluctance motors at the same output power. Since the topology exists for longer than 100 years, many ways to optimise it have already been investigated. Despite the great age of the topology, it is still a challenging task to calculate the so called additional losses. These losses arise in real induction motors and can't be measured in a direct way. Their amount can differ between 0.5% and 5% of the motors input power.

In skewed motors, a part of these losses is connected to the phenomena of inter-bar currents. They flow between adjacent bars inside the rotor lamination. On their way they stream through a contact resistance between bar and iron, then through the resistance of the iron and finally again through a contact resistance between the iron and the neighboring bar. By this, resistive losses are generated in the iron as well as in the transitions between the bars and the iron. The theoretical background can be studied for example in [1], [2], [3], [4] and others.

III. FEM Model

A. Partial Differential Equation

In order to recieve the distribution of the magnetic vector potential as well as the electric scalar potential in an induction motor, one has to solve an eddy current problem. For time harmonic approaches and in case of fields which change slowly over time, the partial differential equation to be solved is then given with

$$\vec{\nabla} \times \tilde{\mu}^{-1} \left(\vec{\nabla} \times \underline{\vec{A}} \right) = -j\omega\tilde{\kappa}\underline{\vec{A}} - \tilde{\kappa}\vec{\nabla}\underline{\varphi} + \vec{J}_\mathrm{e}. \tag{1}$$

For this case, the current density results in

$$\underline{\vec{J}} = \tilde{\kappa}\vec{E} + \vec{J}_\mathrm{e} \tag{2}$$

with the electric field

$$\underline{\vec{E}} = -j\omega\underline{\vec{A}} - \vec{\nabla}\underline{\varphi}. \tag{3}$$

To solve the partial differential equation (1) in COMSOL, the Magnetic and Electric Fields interface from the ACDC-module can be used.

B. Geometry

The model's geometry consists of the induction motor's rotor, the airgap and the air regions in the end area of the motor. Using the theory from [5], the stator is replaced by a Neumann boundary condition and does not need to be modeled geometrically. The rotor consists of 28 slots. Their shape is shown in figure 2. The squirrel cage is made of almunium and the rotor is skewed by 19.3 degrees.

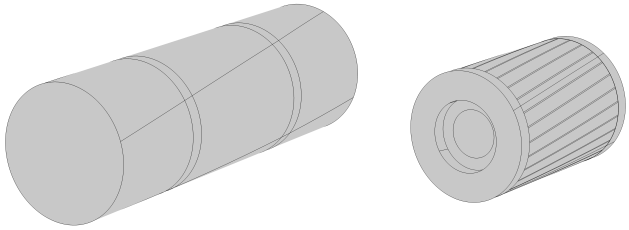

Figure 1: Visualisation of the geometry. The motor's rotor on the right side is hidden within the surrounding air domains on the left side.

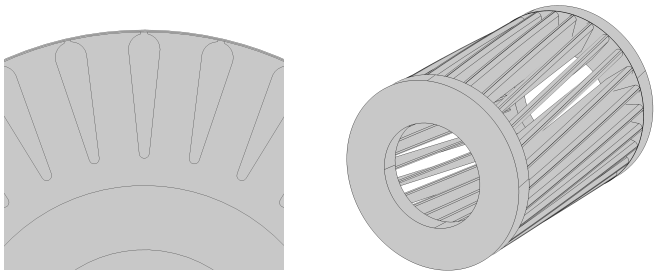

Figure 2: The view of the cutted geometry on the left side shows the slot shape while the skewing of the squirrel cage is indicated on the right side.

C. Boundary Conditions

To be able to solve the equation system, which results from (1), additional constraints for the solving variables need to be used at the outer boundaries of the geometry. According to (1) the solving variables are the magnetic vector potential and the electric scalar potential. A Dirichlet condition is used on the face boundaries in the end areas, which forces the value of both, the magnetic vector potential and the scalar potential to zero.

$$\underline{\vec{A}} = 0 \tag{4}$$

$$\underline{\varphi} = 0 \tag{5}$$

The different coordinate systems are shown in figure 3. It

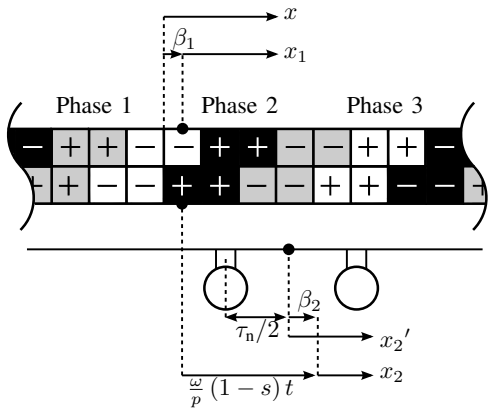

Figure 3: different coordinate systems

shows the coordinate systems, that are fixed to the stator, as well as the systems, that are fixed to the rotor. Since no stator geometry is modeled, the influence of it's magnetomotive force is taken into account by the use of a Neumann boundary condition with

$$\vec{\nabla}\underline{\vec{A}} \cdot \vec{n} = \mu \underline{\vec{j}}_{\mathrm{s}}. \tag{6}$$

Starting from a known stator winding and current, the surface current density is derived from the magnetomotive force. The derivations in [5] lead to a surface current density above the rotor iron for $|z| < l_{\mathrm{z}}/2$ in figure 4 with

$$^{\nu}\underline{\vec{j}}_{\mathrm{s,fe}}(x_2) = \begin{bmatrix} 0 \\ 0 \\ -j\nu\, ^{\nu}c\,\sqrt{2}\underline{I}_1 \exp j\left[^{\nu}s\omega t - \nu x_2\right] \end{bmatrix}. \tag{7}$$

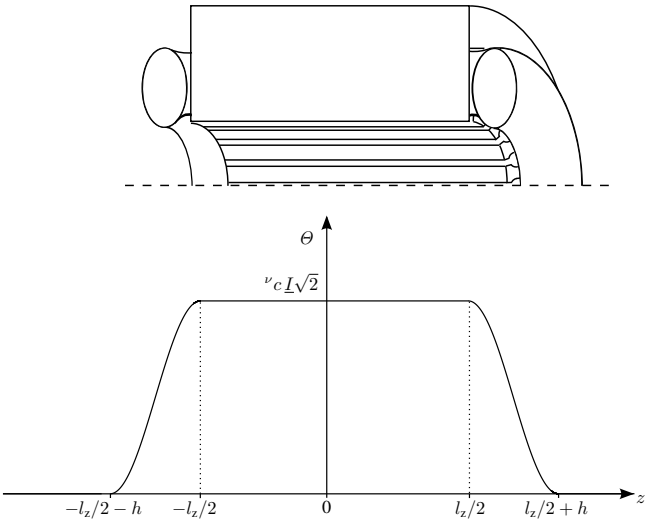

Figure 4: magnetomotive force in the y,z-plane

Since the current density is solenoidal, the surface current density in the end area for $l_{\mathrm{z}}/2 + h > |z| > l_{\mathrm{z}}/2$ can be

expressed by

$$\underline{\vec{j}}_{\mathrm{s,air}}^{\,\nu}(x_2,z)=\begin{bmatrix}0\\ -\sin\left[\pi/h(z-l_\mathrm{z}/2)\right]/2\cdot w\,{}^{\nu}c\sqrt{2}\underline{I}_1\\ \cdot\exp j\left[{}^{\nu}s\omega t-\nu x_2\right]\\ -j\nu\,{}^{\nu}c\sqrt{2}\underline{I}_1\cdot\left(\cos\left[\pi/h(z-l_\mathrm{z}/2)\right]+1\right)/2\\ \cdot\exp j\left[{}^{\nu}s\omega t-\nu x_2\right]\end{bmatrix}. \quad (8)$$

D. Transition Condition

To simulate a contact impedance as a transition boundary condition, the expression for the current density in the boundary can be written as

$$\vec{n}\cdot\vec{J}=\left(\frac{1}{r_\mathrm{q}}+j\omega C_\mathrm{q}\right)\cdot(\varphi_1-\varphi_2) \quad (9)$$

with r_q being the surface resistivity, C_s as the surface capacity and $\Delta\varphi$ as the voltage drop between the inner and outer wall of the boundary. To investigate the influence of the inter-bar

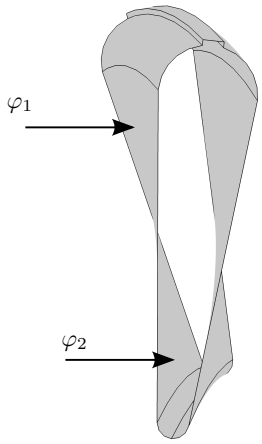

Figure 5: the surface resistance causes a potential difference between the inner and the outer wall of the skewed slot.

resistance, the slot walls, which are shown in figure 5, are defined as contact resistivity. The capacity of the inter-bar impedance is neglected which leads to

$$C_\mathrm{q}=0. \quad (10)$$

E. Material Properties

The material properties are taken from [5]. The rotor lamination is replaced by a single domain. The electric conductivity of this domain is set to zero in axial direction, while it stays untouched in every other direction.

$$\tilde{\kappa}_\mathrm{iron}=\begin{pmatrix}\kappa_\mathrm{xx}&\kappa_\mathrm{xy}&\kappa_\mathrm{xz}\\ \kappa_\mathrm{yx}&\kappa_\mathrm{yy}&\kappa_\mathrm{yz}\\ \kappa_\mathrm{zx}&\kappa_\mathrm{zy}&\kappa_\mathrm{zz}\end{pmatrix}=\begin{pmatrix}\kappa_\mathrm{fe}&0&0\\ 0&\kappa_\mathrm{fe}&0\\ 0&0&0\end{pmatrix} \quad (11)$$

The influence of the small air portions between the lamination sheets on the magnetic conductivity is respected by a substitution permeability μ'. This leads to very low permeability values in axial direction, depending on the stacking factor k_s.

$$\mu'=\frac{\mu_0}{k_\mathrm{s}\left(\frac{1}{\mu_\mathrm{r}}-1\right)+1} \quad (12)$$

Overall, the permeability matrix of the rotor domain looks like

$$\tilde{\mu}_\mathrm{iron}=\begin{pmatrix}\mu_\mathrm{xx}&\mu_\mathrm{xy}&\mu_\mathrm{xz}\\ \mu_\mathrm{yx}&\mu_\mathrm{yy}&\mu_\mathrm{yz}\\ \mu_\mathrm{zx}&\mu_\mathrm{zy}&\mu_\mathrm{zz}\end{pmatrix}=\begin{pmatrix}\mu_\mathrm{fe}&0&0\\ 0&\mu_\mathrm{fe}&0\\ 0&0&\mu'\end{pmatrix}. \quad (13)$$

F. Voltage calculation

Starting from the general voltage equation of a coil

$$\underline{U}=R\underline{I}+j\omega\underline{\Psi}, \quad (14)$$

the voltage equation of one stator phase can be derived with

$$\underline{U}=R_1\underline{I}_1+j\omega\underline{\Psi}_1. \quad (15)$$

The flux linkage of one phase is made up out of the two parts

$$\underline{\Psi}_1=\underline{\Psi}_\sigma+\underline{\Psi}_\delta. \quad (16)$$

The first component describes the flux linkage, which is linked to the leakage of the stator phase. It is composed out of three parts with

$$\underline{\Psi}_\sigma=\underline{\Psi}_{\sigma,\mathrm{d1}}+\underline{\Psi}_{\mathrm{N1}}+\underline{\Psi}_{\mathrm{S1}}. \quad (17)$$

They describe the leakage of the airgap field, the stator slots and the winding heads. Since the stator of this model is considered analytical, while the rotor is modeled numerically, the flux linkage $\underline{\Psi}_\sigma$ needs to be expressed as a multiplication of the current and an inductance

$$\underline{\Psi}_\sigma=L_{\sigma,1}\underline{I}=\left(L_{\sigma,\mathrm{d1}}+L_{\mathrm{N1}}+L_{\mathrm{S1}}\right)\underline{I}_1. \quad (18)$$

The second flux linkage component in (16) derives from the airgap field. In order to recieve this from the numerical model, the flux of the first phase needs to be calculated with

$$\underline{\Phi}_\mathrm{pole}=\iint_{\text{pole area}}\underline{\vec{B}}_\delta\,\mathrm{d}\vec{a}. \quad (19)$$

To get the flux linkage, the flux has to be multiplied by the number of turns per phase and the winding factor

$$\underline{\Psi}_\delta=k_\mathrm{w}w\,\underline{\Phi}_\mathrm{pole}. \quad (20)$$

Equation (15) can then be replaced by

$$U=\left(R_1+j\omega L_{\sigma,1}\right)\cdot\underline{I}_1+j\omega\underline{\Psi}_\delta. \quad (21)$$

G. Mesh

Since the change of the solving variables in axial direction is rather small in the iron region, the use of a sweeped mesh can be beneficial. Figure 6 shows the sweeped mesh in a cut view. It is sweeped with respect to the skewing of the rotor. The figure also shows that the mesh in the end areas is chosen coarse and built without sweep. Overall, the mesh consists of 640000 elements.

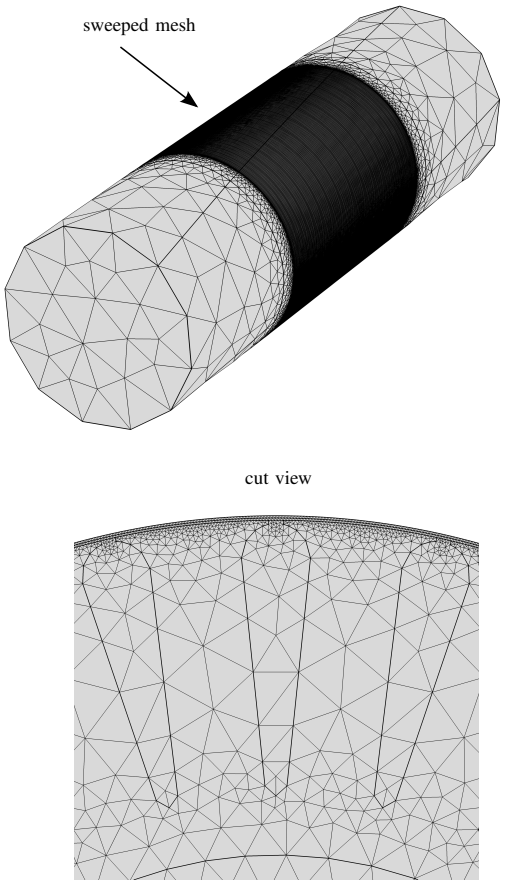

Figure 6: Mesh overview

IV. Results

A. Verification

The first result is a presentation of the validation without inter-bar currents. In this case, the inter-bar resistance as well as the iron permeability are set to infinity. The 3D model should then deliver the same motor behaviour as the fundamental model from [6]. According to figure 7, analytical and numerical

$U_{1,2}$ [V]	100
f [Hz]	50
$\nu_{\max}$ [1]	2
$\mu_{\mathrm{r,Fe}}$ [1]	∞
k_{s} []	1
r_{q} [Ω/m^2]	∞

Table I: Simulation parameters of the verification

calculations of the torque match well. This means that the additions to [5], which are the voltage equations, the flux calculation, the introduction of the electric scalar potential, seem to be done right.

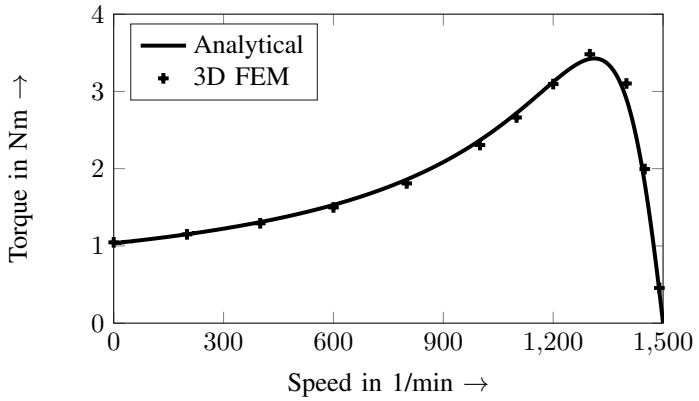

Figure 7: Verification of the 3D model with analytical results

B. Inter-bar currents and stacking

The next series of simulations is a two dimensional parametric study. The first parameter is the stacking factor k_{s} with the values 0.94, 0.96 and 0.98. The second parameter is the inter-bar resisitivity r_{q}, which varies between $10^{-1}\Omega/\mathrm{m}^2$ and $10^{-12}\Omega/\mathrm{m}^2$. The results show that the torque behaviour of all

$U_{1,2}$ [V]	100
f [Hz]	50
$\nu_{\max}$ [1]	2
$\mu_{\mathrm{r,Fe}}$ [1]	500
k_{s} []	0.94...0.98
r_{q} [Ω/m^2]	$10^{-1}...10^{-12}$

Table II: Simulation parameters of the stacking simulation

three different stacking factors is similar. Small differences can be detected for $r_{\mathrm{q}} = 1e-6\Omega/\mathrm{m}^2$. The torque is higher for low speed values in case of low stacking factors. The basic torque-speed behaviour and the influence of different inter-bar resistances is generally the same for all stacking factors. The additional losses in the iron domain and in the transition boundaries raise the torque. This effect is dominant at low speed values. The solutions also show, that the torque for standstill has a maximum at about $r_{\mathrm{q,worst\text{-}case}} = 1e-6\ \Omega/\mathrm{m}^2$. Bigger and smaller values of r_{q} lead to a lower torque. This does not only count for standstill, but also for lower speeds. As a result of this, manufactured motors, with a r_{q} close to $r_{\mathrm{q,worst\text{-}case}}$ can show inconstancies in their operational behaviour, because r_{q} strongly depends on the production process of the rotor.

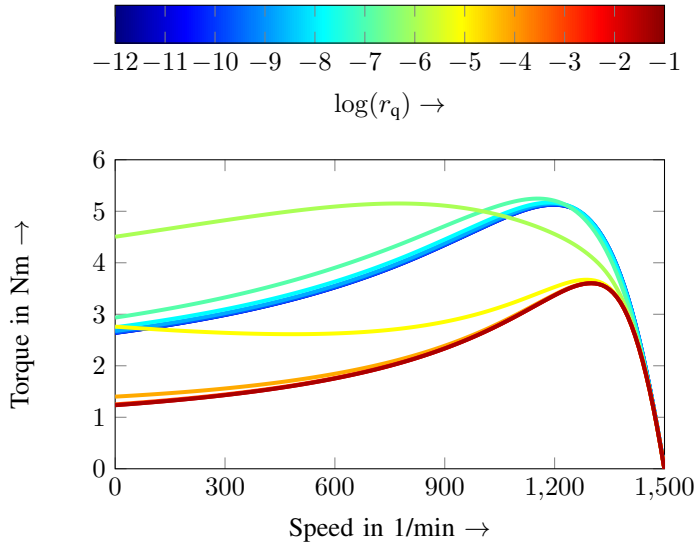

Figure 8: Torque vs speed curve for a stacking factor of k_s=0.94

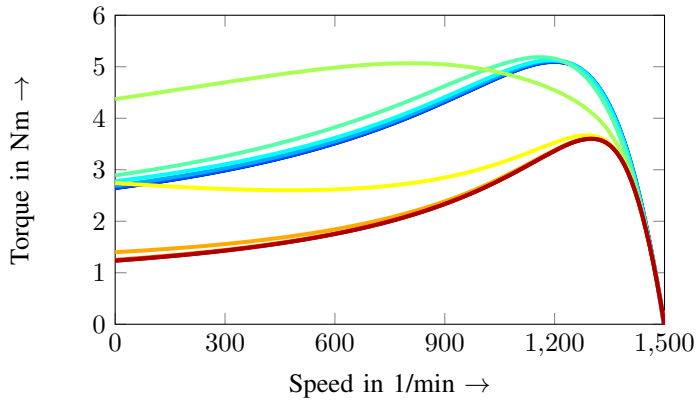

Figure 9: Torque vs speed curve for a stacking factor of k_s=0.96

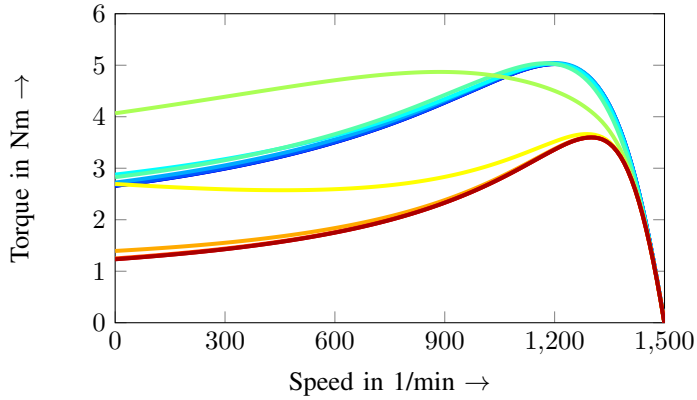

Figure 10: Torque vs speed curve for a stacking factor of k_s=0.98

V. Conclusions

The numerical model from [5] was extended by the consideration of a voltage equation, the flux calculation and the implementation of the electric scalar potential. Latter was done to consider the inter-bar resistance as a transition boundary condition instead as a transition domain with a specific electric conductivity. This helps to save some effort to solve the model, since the thin transition domains needed a relatively fine mesh. The validation of the new model compared to the analytical results show that the implementations were programmed correctly. The chosen approach to include the rotor lamination shows that different values of the stacking factor do only have a very small influence on the inter-bar-current behavior. Other than in [5], the investigations have been made at constant voltage instead of impressed currents.

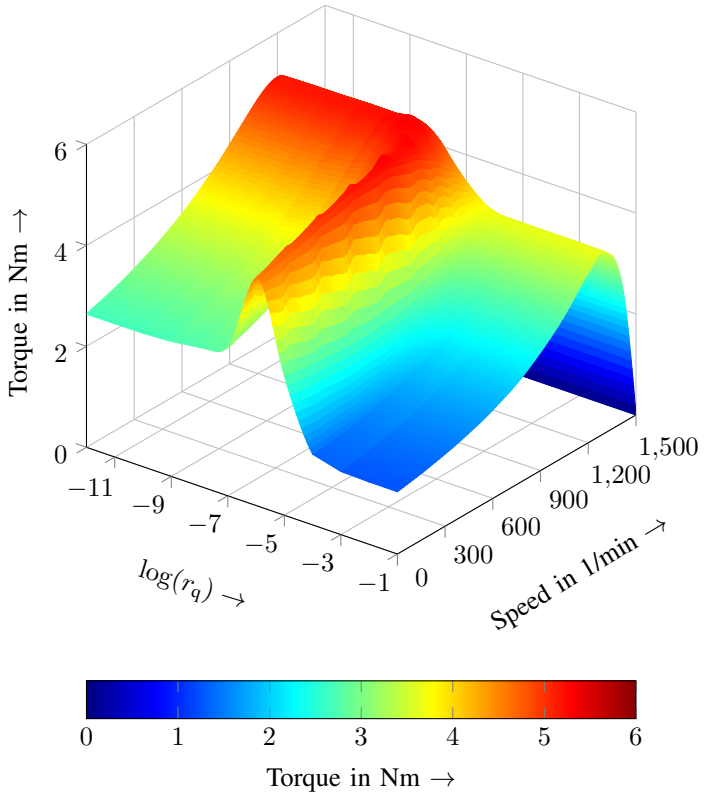

Figure 11: Alternative visualisation of figure 8

References

[1] A. Odok, *Zusatzverluste und Zusatzmomente in Kurzschlussankermotoren mit unisolierten Stäben. Diss. Nr. 2437 techn. Wiss. ETH Zürich*. 1955.

[2] V. Roßmaier, "Berechnung der durch unisolierte Käfige hervorgerufene Zusatzverluste bei Asynchronmaschinen," *Elektrotechnik und Maschinenbau*, pp. 249–255, 1939.

[3] W. Wagner, *Berechnung von Drehstromasynchronmaschinen mit Käfigläufern unter Berücksichtigung von mehrfacher Ankerrückwirkung, Nutenöffnungen und Rotorquerströmen*. Dissertation of the University Dortmund, 1986.

[4] R. Weppler, "Ein Beitrag zur Berechnung von Asynchron-

motoren mit nichtisoliertem Läuferkäfig," *Archiv für Elektrotechnik*, pp. 238–252, 1966.
[5] J. Güdelhöfer, R. Gottkehaskamp, and A. Möckel, "3D FEM Approach to Study the Physics of Inter-bar Currents in Induction Machines," *XXII International Conference on Electrical Machines ICEM*, 2016.
[6] W. Nürnberg, *Die Asynchronmaschine: ihre Theorie und Berechnung unter besonderer Berücksichtigung der Keilstab- und Doppelkäfigläufer*. Springer, 1963.

VI. Biographies

Jan Güdelhöfer received the B.Sc. and M.Sc. degrees in electrical engineering from the University of Applied Sciences Düsseldorf, Düsseldorf, Germany, in 2011 and 2013, respectively. Since 2012, he has been with the Laboratory for Electromagnetic Field Theory and Electrical Machines, Faculty of Electrical and Information Technology, University of Applied Sciences Düsseldorf, as a Research Associate. His current research interests include the field of the electromagnetic design and modelling of synchronous and asynchronous machines.

Raimund Gottkehaskamp received the Dipl. Ing. and Dr. Ing. degrees in electrical engineering from the University of Dortmund, Dortmund, Germany, in 1987 and 1992, respectively. From 1992 to 1997 he worked for the Company Groschopp AG in Viersen, Germany, in different R&D and management positions. Most recently, he was responsible for research and development of small electrical machines. Since 1997, he is a member of the Faculty of Electrical and Information Technology of the University of Applied Sciences Düsseldorf, Germany and heads the Laboratory for Electromagnetic Field Theory and Electrical Machines. His fields of interest are numerical and analytical modelling of magnetic circuits in electrical machines and other devices, especially field harmonic theories of synchronous and asynchronous machines.

Andreas Möckel received his Diploma in Electrical Engineering, the Ph.D. degree and the habilitation from the Technische Universität Ilmenau, Germany. Since 2006, he is head of the Small Electrical Drives Group (TU Ilmenau) and supports Ph.D. students on the various fields of electrical machines. The Group concentrates on the development of brushed and brushless motors.